Dissolution and Recrystallization Behavior of Li_3PS_4 in Different Organic Solvents with a Focus on N-Methylformamide

Wissel, Kerstin; Riegger, Luise M.; Schneider, Christian; Waidha, Aamir I.; Famprikis, Theodosios; Ikeda, Yuji; Grabowski, Blazej; Dinnebier, Robert E.; Lotsch, Bettina V.; Janek, Jürgen

DOI
10.1021/acsaem.2c03278

Publication date
2023

Document Version
Final published version

Published in
ACS Applied Energy Materials

ACS APPLIED ENERGY MATERIALS

www.acsaem.org Article

Dissolution and Recrystallization Behavior of Li_3PS_4 in Different Organic Solvents with a Focus on *N*-Methylformamide

Kerstin Wissel,* Luise M. Riegger, Christian Schneider, Aamir I. Waidha, Theodosios Famprikis, Yuji Ikeda, Blazej Grabowski, Robert E. Dinnebier, Bettina V. Lotsch, Jürgen Janek, Wolfgang Ensinger, and Oliver Clemens

Cite This: *ACS Appl. Energy Mater.* 2023, 6, 7790−7802 Read Online

ACCESS | Metrics & More | Article Recommendations | Supporting Information

ABSTRACT: Solid-state batteries can be built based on thiophosphate electrolytes such as β-Li_3PS_4. For the preparation of these solid electrolytes, various solvent-based routes have been reported. For recycling of end-of-life solid-state batteries based on such thiophosphates, we consider the development of dissolution and recrystallization strategies for the recovery of the model compound β-Li_3PS_4. We show that recrystallization can only be performed in polar, slightly protic solvents such as *N*-methylformamide (NMF). The recrystallization is comprehensively studied, showing that it proceeds via an intermediate phase with composition Li_3PS_4·2NMF, which is structurally characterized. This phase has a high resistivity for the transport of lithium ions and must be removed in order to obtain a recrystallized product with a conductivity similar to the pristine material. Moreover, the recrystallization from solution results in an increase of the amorphous phase fraction next to crystalline β-Li_3PS_4.

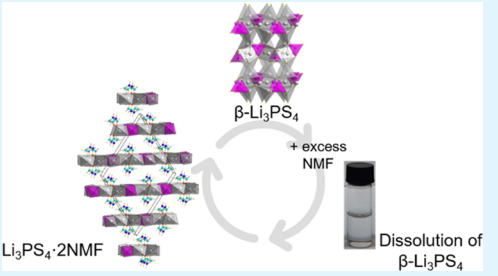

KEYWORDS: *thiophosphate, β-Li_3PS_4, solvent treatment, recrystallization, N-methylformamide, recycling*

1. INTRODUCTION

Inherent safety concerns related to the use of combustible liquid electrolytes and limited energy density of commercial lithium-ion batteries (LIBs) have prompted the development of different next-generation battery technologies, of which all-solid-state batteries (ASSBs) utilizing solid electrolytes (SEs) are regarded to be highly promising. Various material classes (e.g., oxides, halides, and sulfides) are currently being investigated for their use as SE. Among these, sulfides show some of the highest room-temperature ionic conductivities (up to $\approx 10^{-2}$ S/cm).[1] Prominent examples of these sulfide SEs are Li−P−S (LPS)-based glasses or glass ceramics (e.g., $x$$Li_2S$·$(100-x)$$P_2S_5$, $Li_7P_3S_{11}$, β-Li_3PS_4), argyrodites Li_6PS_5X (X = Cl, Br, I), thio-LISICONs, or $Li_{11-x}M_{2-x}P_{1+x}S_{12}$ (M = Ge, Sn, Si). β-Li_3PS_4, $Li_7P_3S_{11}$, and argyrodites can be obtained via scalable liquid-phase syntheses. For example, β-Li_3PS_4 can be synthesized when its precursors Li_2S and P_2S_5 are either dissolved or dispersed in different organic solvents. Commonly used solvents for the synthesis are, e.g., acetonitrile (ACN),[2] diethylene glycol dimethyl ether (DEGDME),[3] dimethyl carbonate (DMC),[4] dimethoxyethane (DME),[5] ethyl acetate (EA),[6] ethylenediamine (EDA),[7] *N*-methylformamide (NMF),[8−10] or tetrahydrofuran (THF).[11] During the synthesis, the precipitation of Li_3PS_4 complexated with the respective solvent (e.g., Li_3PS_4·ACN,[12] Li_3PS_4·DME,[5] Li_3PS_4·2EA,[6] Li_3PS_4·3THF[11]) takes place. After an additional thermal treatment to remove the solvent, β-Li_3PS_4 crystallizes from these complexes.[12]

With the expected commercialization of ASSBs, sustainable battery recycling strategies will be of rising urgency. However, to date, most of the recycling research efforts focus on traditional LIBs with organic liquid electrolytes and are based on pyrometallurgical and/or hydrometallurgical processes, aiming at the recycling of the valuable metals (predominantly Ni, Co, Mn) contained exclusively in the electrode materials. Irrecoverable losses of the liquid electrolytes and lithium lower the overall material recovery rate drastically, while the energy and cost efficiency remain low as well. As ASSBs are still under development, there is great opportunity to early on establish economically viable and efficient recycling strategies taking also sustainable battery design concepts with a focus on the recyclability of such batteries into account. Owing to the potential for solution processing of sulfide electrolytes, sulfide-based ASSBs might offer significant potential in this respect since direct recycling concepts involving the dissolution and recrystallization of the electrolyte could be adopted.[13] This way, the insoluble electrode materials could be separated via filtration or centrifugation from the dissolved electrolyte and processed

Received: October 7, 2022
Accepted: July 5, 2023
Published: July 25, 2023

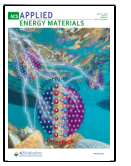

https://doi.org/10.1021/acsaem.2c03278
ACS Appl. Energy Mater. 2023, 6, 7790−7802

separately. So far only little is known on the recycling of sulfide electrolytes: Tan et al.[14] reported on a potential recycling strategy for thiophosphate electrolyte-based Li|Li_6PS_5Cl|$LiCoO_2$ cells employing ethanol as solvent allowing for a separation of $LiCoO_2$ from the formed suspension. After the removal of the solvent, Li_6PS_5Cl could be recovered.

A key requirement for this recycling strategy is that the electrolyte is fully dissolvable, while avoiding a chemical degradation of the electrolyte when in solution. In this context, it has been noted that polar solvents readily solvate thiophosphate units.[13,15] Keeping thiophosphate units intact is essential, although it can be difficult since sulfide electrolytes show a high reactivity toward most solvents. It should be noted that dissolution strategies must be conceptionally distinguished from synthesis strategies, as not precursor materials but sulfide electrolytes have to be processed in the solvent. For β-Li_3PS_4, there is a large number of studies on solvent-based processing in the context of the preparation of active electrode coatings, composite electrodes, or separator films; however, most of these studies start from the precursor Li_2S and P_2S_5 (or glassy $75Li_2S{\cdot}25P_2S_5$ (mol %)) and/or use nonpolar or weakly polar aprotic solvents only.[16−24] Thus, the present study aims to investigate the impact of solvent treatments on β-Li_3PS_4. For this, a variety of solvents covering a broad range of physical and chemical properties are systematically screened and the solubility of β-Li_3PS_4 within them is investigated. Structural and chemical changes of the precipitated phases formed after the removal of the solvent are examined using X-ray diffraction (XRD) and Raman spectroscopy. A detailed investigation on the recrystallization behavior of β-Li_3PS_4 after complete dissolution in NMF is carried out. The formation of a previously unreported $Li_3PS_4{\cdot}$2NMF complex is observed, which is determined to have a *C*-centered monoclinic crystal structure in the space group $C2/c$. Effects of the dissolution in NMF on the obtained materials are investigated via a combination of X-ray and neutron diffraction, Rietveld analysis, and X-ray photoelectron (XPS), infrared (IR), and electrochemical impedance (EIS) spectroscopy. Morphology changes are followed using scanning electron microscopy (SEM).

2. EXPERIMENTAL SECTION

2.1. Material Preparation. The pristine electrolyte β-Li_3PS_4 was purchased from NEI Co. Material handling and preparation were carried out in an inert atmosphere.

To investigate the effect of solvent treatment on β-Li_3PS_4, different organic solvents including hexane (anhydrous, Alfa Aesar), toluene (anhydrous, 99.8%, Sigma-Aldrich), tetrahydrofuran (THF, anhydrous, 99.8+ %, Alfa Aesar), ethyl acetate (EA, 99.8%, Sigma-Aldrich), 1,2-dimethoxyethane (DME, anhydrous, 99.5%, Sigma-Aldrich), acetonitrile (ACN, anhydrous, 99.8+%. Alfa Aesar), *N*-methylformamide (NMF, 99%, Thermo Scientific), isopropanol (*i*-PrOH, anhydrous, max. water 0.003%, VWR Chemicals), ethanol (EtOH, anhydrous, max. water 0.003%, VWR Chemicals), and methanol (MeOH, anhydrous, 99.9%, Thermo Scientific) were selected. This selection covers a variety of solvents that are commonly used in the literature for the synthesis of β-Li_3PS_4, i.e., THF, EA, DME, and ACN (polar, aprotic), NMF (polar, (weakly) protic), as well as other nonpolar solvents (i.e., hexane and toluene) and polar, stronger protic solvents (i.e., *i*-PrOH, EtOH, and MeOH). The physical and chemical properties of the used solvents are summarized in Table S1. The solvents were dried over a molecular sieve (3 Å, 20% m/v, Sigma-Aldrich). The molecular sieve was removed from the solvent after 72 h via filtration. To avoid any contamination from colloidal molecular sieve particles within the solvent, vacuum distillation was carried out in addition. The water contents of the solvents were determined by Karl Fischer titration (Titrator Compact C10SX, Mettler Toledo) and are also given in Table S1. 250 mg of the electrolyte were mixed with 50 mL of solvent under Ar atmosphere. After 4 h of stirring, the Schlenk flasks were connected to a Schlenk line and heated to 120 °C under vacuum ($p \approx 1-3 \times 10^{-2}$ mbar) for 4 h to remove the respective excess solvent. For ACN, DME, and NMF, additional heat treatments of the obtained powders were performed at 240 °C for 4 h in a vacuum oven (glass oven B-585 drying, Büchi). For *i*-PrOH, EtOH, and MeOH, additional heat treatments were conducted at 550 °C (heating to 240 °C did not result in significant changes of the samples). For this, the powders were sealed in evacuated glass ampoules and heated to 550 °C for 12 h.

For further dissolution experiments with NMF, different β-Li_3PS_4 to NMF solid-to-liquid ratios were investigated. Using a ratio of 50 mg to 1 mL and a stirring time of 30 min, 3 g of β-Li_3PS_4 was dissolved in NMF and the sample was heated to a temperature of 120 °C at a pressure of $\sim 2 \times 10^{-2}$ mbar for 4 h. This sample was subsequently divided into several samples, and each one was heated to a temperature between 140 and 300 °C under vacuum ($p \approx 1-5 \times 10^{-2}$ mbar) for additional 4 h.

2.2. Characterization. *2.2.1. X-ray and Neutron Powder Diffraction and Rietveld Analysis.* XRD patterns were recorded on a Rigaku SmartLab in Bragg−Brentano geometry with Cu Kα radiation with a wavelength of 1.542 Å and a Hypix-3000 detector. Samples were measured inside low-background airtight sample holders (Rigaku), which were sealed inside an Ar-filled glovebox.

Neutron powder diffraction (NPD) experiments were performed at the PEARL diffractometer of the Reactor Institute Delft (TU Delft, the Netherlands).[25] Approximately 600 mg of sample was loaded in a 6 mm diameter can made of V−Ni null-scattering alloy, which was sealed airtightly using a rubber O-ring. Handling of the powder was performed in an Ar-filled glovebox. The sample can was placed in a neutron-transparent vacuum box connected to primary vacuum ($\sim 10^{-3}$ mbar). The diffractogram was measured over ~21 h using a wavelength of 1.667 Å selected using the (533) reflection of a Ge[511] monochromator. The instrument background determined from measurements of the empty can was subtracted from the raw diffractogram. Detector pixel normalization was performed by fitting a measurement of a PMMA rod in the same configuration.

Analysis of diffraction data was performed via the Rietveld method with the program TOPAS V.6.0. For the crystal structure determination, a coupled Rietveld analysis of X-ray and neutron powder diffraction data was performed. The instrumental intensity distribution of the XRD and NPD instruments were determined empirically from a fundamental parameter set determined using a reference scan of LaB_6 (NIST 660a) and Al_2O_3 (NIST 676a), respectively. Microstructural parameters (i.e., crystallite size and strain broadening) were refined to adjust the peak shapes.

For the determination of amorphous phase contents, the samples were mixed in a defined weight ratio with Al_2O_3 (calcinated at 1100 °C) and XRD patterns were recorded. The calculation of the respective amorphous fraction was performed using the internal standard method as implemented in TOPAS V.6.0.

2.2.2. Thermogravimetric and Evolved Gas Analysis. To quantify the amount of solvent in $Li_3PS_4{\cdot}x$NMF, thermogravimetric analysis (TGA) was performed. Furthermore, evolved gas analysis (EGA) was performed to identify the compounds released during TG analysis. Prior to the TGA/EGA measurement, blank samples were measured to minimize buoyancy effects in the TGA and to obtain background spectra in the EGA. For the TGA measurement, about 10 mg of $Li_3PS_4{\cdot}x$NMF powder sample was loaded into an Al_2O_3 crucible and subsequently transferred into the furnace chamber. The TGA was carefully purged several times with helium to avoid atmospheric contaminates. The sample was heated with a heating rate of 10 K min^{-1} to 300 °C (Netzsch Jupiter STA 449 F3, SiC furnace, type S thermocouple sample carrier, 70 ml min^{-1} He (5N Air Liquid) stream). The TGA data were analyzed with the software Proteus Analysis (Netzsch). Sampling of the evolved exhaust gas was performed at 86, 212, and 278 °C. The sampled gas was transferred via an inert, heated line to a gas chromatograph (GC, Agilent 8890 GC System, HP-5MS UI column with 30 m × 0.25 mm × 0.25 μm, 20:1 injection split ratio, sample inlet temperature 300 °C, He carrier with 1.2 mL min^{-1}). The

https://doi.org/10.1021/acsaem.2c03278
ACS Appl. Energy Mater. 2023, 6, 7790−7802

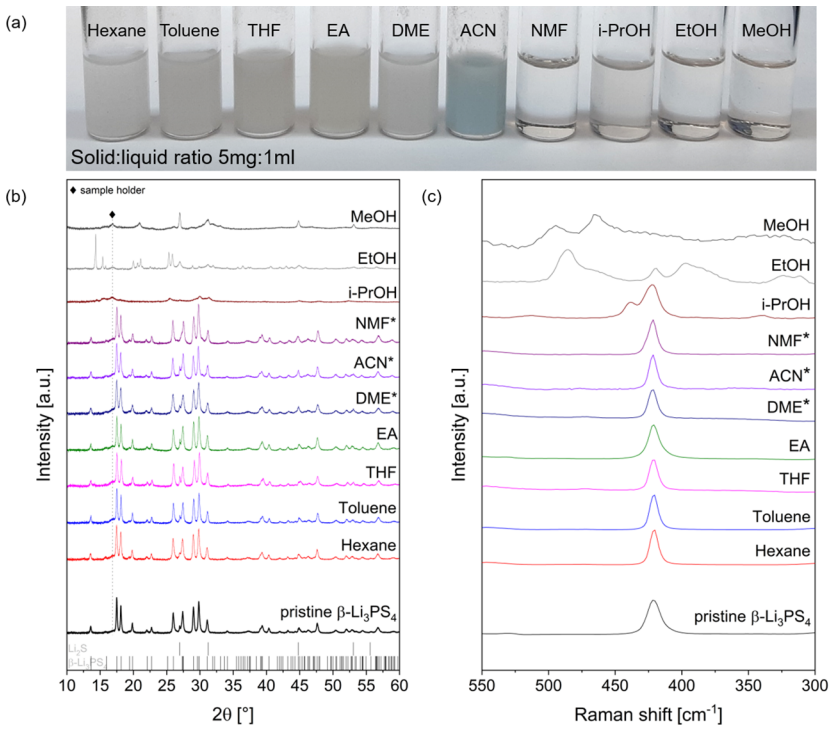

Figure 1. (a) Photograph of β-Li_3PS_4 in different organic solvents (solid:liquid ratio 5 mg/1 mL). (b, c) X-ray diffraction patterns and Raman spectra of dried precipitates obtained after solvent treatment of β-Li_3PS_4 in organic solvents in comparison to pristine β-Li_3PS_4. To remove the solvents, the samples were heated to 120 °C for 4 h at reduced pressures. To decompose Li_3PS_4·solvent complexes (Figure S1), samples marked with * were additionally heated to 240 °C for 4 h at reduced pressures. The positions of the characteristic reflection ticks of β-Li_3PS_4 and Li_2S are given in black and gray, respectively.

GC oven was set to a constant temperature of 100 °C. After passing the GC, the separated components were detected in a mass spectrometer (MS, Agilent 5977B GC/MSD, EI mode, 230 °C ion source temperature, 150 °C quadrupole temperature). The total ion current of the GC peaks was measured. The mass spectra were analyzed by means of best-matching database entries (NIST database, MSD ChemStation Data Analysis).

2.2.3. DFT Calculations. To further support the atomic positions determined in the Rietveld analysis, structural optimization based on ab initio density functional theory (DFT) was also conducted. The optimization was done for the primitive cell including 52 atoms, where the primitive lattice vectors are $(\boldsymbol{a} - \boldsymbol{b})/2$, $(\boldsymbol{a} + \boldsymbol{b})/2$, and $\boldsymbol{c}$. The DFT calculations were performed using the VASP code.[26−28] with the plane-wave basis projector augmented wave (PAW) method.[29] The exchange−correlation energy was obtained within the generalized gradient approximation (GGA) of the Perdew−Burke−Ernzerhof (PBE) form.[30] The plane-wave cutoff energy was set to 520 eV. Reciprocal spaces were sampled by a Γ-centered $6 \times 6 \times 3$ k-point mesh and the tetrahedron method with the Blöchl correction.[31] H 1s, Li 2s, C 2s2p, N 2s2p, O 2s2p, P 3s3p, and S 3s3p orbitals were treated as the valence states. Total energies were minimized until they converged within 1×10^{-6} eV per simulation cell for each ionic step. Cell volume, cell shape, and internal atomic positions were optimized so that the forces on atoms and the stress components on the unit cell became less than 1×10^{-2} eV/Å and 1×10^{-4} eV/Å^3, respectively.

2.2.4. Scanning Electron Microcopy. SEM images were recorded using a secondary electron detector of an FEI Quanta 250 SEM operating at 30 keV. Prior to the measurements, a layer of Au was sputtered onto the samples.

2.2.5. Raman Spectroscopy. Raman spectra were recorded with a confocal micro-Raman spectrometer Horiba HR 800 equipped with a laser wavelength of 532 nm. For calibration of the spectrometer, the 521 cm^{-1} Stokes signal of a silicon wafer was used. Calibration measurements were performed after each measurement. Samples were measured in glass capillaries sealed under an inert atmosphere.

2.2.6. Infrared Spectroscopy. Fourier-transform infrared (FTIR) spectroscopy measurements were conducted on a Varian spectrometer. Samples were characterized via attenuated total reflection (ATR) using an ATR unit (Specac) equipped with a reactive sample anvil. For the sample preparation, the ATR unit was transferred into an Ar-filled glovebox, where the sample was compressed under an inert atmosphere, sealing the powder from the environment with an O-ring. To limit the duration of possible exposure to air, the measurement was conducted as quickly as possible after the unit was transferred out of the glovebox.

2.2.7. X-ray Photoelectron Spectroscopy. XPS measurements were carried out on a PHI 5000 VersaProbe II Scanning ESCA Microprobe (Physical Electronics GmbH) with a monochromatized Al Kα source (1486.6 eV). The beam had a power of 50 W and a diameter of 200 μm. The sample surface was charge-neutralized with slow argon ions and electrons. Ar^+ ions accelerated with 0.5 kV were used to sputter a depth profile. For the detailed spectra, an analyzer pass energy of 46.95 eV, a step time of 50 ms, and a step size of 0.2 eV were used. CasaXPS software (Casa Software Ltd.) was used for data analysis with a Shirley-type background correction and a GL(30) line shape. Before fitting, all of the peaks were calibrated to the binding energy of adventitious sp^3 carbon (284.8 eV) first. To avoid detrimental surface effects, the spectra were then calibrated to the binding energy of the S 2p main component PS_4^{3-} at 161.7 eV.[32,33]

2.2.8. Electrochemical Impedance Spectroscopy. The conductivity of the obtained materials was measured under pressure in a CompreDrive (rhd instruments). For this, 80 to 100 mg of each powder was loaded into a measuring cell. Carbon-coated aluminum electrodes were used to ensure contact. After applying 380 MPa for 3 min, a constant pressure of 50 MPa was applied during the measurement. It is reasonable to assume based on the activation volumes of chemically similar sulfide electrolytes that the pressure dependence on the bulk ionic conductivity for the used pressure range is negligible.[34−38] The applied pressure mainly serves to provide microstructural densification/consolidation and/or formation/maintenance of good physical/electrical contact with the blocking

https://doi.org/10.1021/acsaem.2c03278
ACS Appl. Energy Mater. 2023, 6, 7790−7802

electrodes. Measurements without applied pressure (Figure S9) support these assumptions. It has to be noted that it was not possible to prepare free-standing pellets of the intermediate phase for measurements without an applied pressure due to severe pellet cracking and delamination.

The thickness of the electrolyte was determined based on the difference in the height between the unfilled cell and the filled cell after the measurement. Electrical impedance measurements were performed using an electrochemical impedance analyzer NEISYS (Novocontrol Technologies) in a frequency range between 7 MHz and 1 Hz with an amplitude of 10 mV in a temperature range between −30 and 100 °C. Received data was analyzed using the software RelaxIS3 (rhd instruments GmbH & Co., KG).

2.2.9. Cyclic Voltammetry. To investigate the electrochemical stability of the electrolytes, cyclic voltammetry was conducted. For this, Li|β-Li_3PS_4|stainless steel cells were prepared, in which Li and stainless steel electrodes served as reference/counter and working electrodes, respectively. 30 mg of pristine or recrystallized β-Li_3PS_4 was uniaxially compacted within a die with a diameter of 7 mm using a handheld hydraulic press (Specac) with 2 t for 3 min. Afterward, Li (thickness 0.75 mm, diameter 5 mm, Sigma-Aldrich) was pressed by hand onto one side of the obtained β-Li_3PS_4 pellet. As counter electrode, the stainless stain current collector of the cell was used. The potential was scanned from −0.5 to 5.0 V vs Li/Li^+ at a scan rate of 5 mVs^{-1}.

3. RESULTS AND DISCUSSION

3.1. Solvent Treatment of β-Li_3PS_4 in Different Organic Solvents. To study the impact of solvent treatment on β-Li_3PS_4, a selection of different organic solvents has been made based on their different physical and chemical properties (Table S1), covering a spectrum from nonpolar over polar aprotic to polar protic solvents. As can be seen in Figure 1a, only the polar protic solvents NMF, *i*-PrOH, EtOH, and MeOH are able to form a clear solution containing a significant quantity of β-Li_3PS_4 (fixed ratios of 5 mg β-Li_3PS_4 per 1 mL of solvent were investigated). However, it should be noted that, while β-Li_3PS_4 is dissolved in less than 2 min in EtOH and MeOH, incomplete dissolution was observed in the case of *i*-PrOH and the mixture remains slightly cloudy.

For all other nonpolar and polar aprotic solvents, a significantly smaller solubility (solubility limits < 0.1 mg/1 mL for hexane, toluene, EA, and DME; <0.5 mg/1 mL for THF and ACN) was found, leading to the presence of considerable amounts of white precipitates. A sedimentation of the particles takes place within 1 to 2 min, showing that stable suspensions cannot be formed. The blue color of the ACN suspension points to a certain reactivity between β-Li_3PS_4 and ACN under the formation of S_3^- radicals,[39,40] while colorless supernatants were observed for the other nonpolar and polar aprotic solvents indicating no to minor reactions between sulfur-containing species and the solvents.[41] The solutions with polar protic solvents have a pale-yellow color.

After the evaporation of the solvents at 120 °C at reduced pressures, the obtained precipitates were collected and X-ray diffraction and Raman spectroscopy measurements (Figure 1b,c) were performed. The orthorhombic crystal structure of β-Li_3PS_4 is recovered for all solvents except for *i*-PrOH, EtOH, and MeOH. It should be noted that the pristine β-Li_3PS_4 contains ∼2 wt % Li_2S as an impurity phase, which is also present in the recrystallized samples. The phase fraction of Li_2S remains constant in all samples.

As has been reported previously when synthesizing β-Li_3PS_4 from DME and ACN,[5,12] insoluble Li_3PS_4·ACN and Li_3PS_4·DME complexes are obtained when using a moderate drying temperature of 120 °C (Figure S1). Only after heating to higher temperatures, these complexes decompose and the formation of β-Li_3PS_4 takes place. A similar behavior is found for NMF suggesting the formation of a so far unknown NMF complex which also transforms to β-Li_3PS_4 at elevated temperatures. The detailed crystal structure and property characterization of this phase is described in Section 3.2. For the alcohols, on the other hand, partial decomposition under the formation of Li_2S and other unknown phases and/or amorphization is observed at this temperature, which is also in agreement with previous studies.[15,42,43] Recrystallization is only possible after heating to higher temperatures. The diffraction patterns obtained after additional heating to 550 °C are shown in Figure S2. The obtained phase mixtures contain large amounts of decomposition products (e.g., Li_3PO_4). Interestingly, alcohols can be used to dissolve and recrystallize successfully other sulfide electrolytes such as argyrodites Li_6PS_5X[43−45] or Li_7PS_6,[42] even though they also contain PS_4^{3-} units. For these electrolytes, the presence of excess Li_2S and/or LiX seems to play an important role in the stabilization of PS_4^{3-} units during the dissolution process. This shows, however, that it is not necessarily possible to dissolve different electrolytes (simultaneously) in a specific solvent, which could become important with respect to potential large-scale recycling considering different thiophosphate-based cell chemistries. Therefore, an additional sorting and separation step would be required. Furthermore, this illustrates that for each sulfide electrolyte that could find application in future ASSB cells, the dissolution behavior has to be studied individually.

The Raman spectra are in excellent agreement with the diffraction data. The signals at ∼421 cm^{-1} dominating the Raman spectra correspond to the symmetric stretching vibration of ortho-thiophosphate units PS_4^{3-},[47] which are expected to be present in the samples showing the β-Li_3PS_4 structure. The decrease of this signal and the appearance of other signals (e.g., polysulfide species in the range ∼450 to 500 cm^{-1}, $P_2S_6^{4-}$ at ∼390 cm^{-1})[43] for the alcohols demonstrates that these samples decomposed significantly. This also confirms findings from previous studies.[41−43]

It can be concluded that only NMF dissolves β-Li_3PS_4 under the retention of the PS_4^{3-} units, making a recrystallization of the crystal structure without considerable visible decomposition possible. Several factors seem to play an important role: NMF is a strongly polar, weakly protic solvent containing NH bonds. The polarity and the weakly positively polarized hydrogen seem to be necessary to solvate the PS_4^{3-} anionic species. In comparison, the alcohols possess OH bonds which make them more nucleophilic. Though this leads to the solvation of the anion, it can also cause decomposition under the formation of $PS_{4-x}(OR)_x$ at the same time since PO bonds are thermodynamically more stable.[15] This reaction step is irreversible and prevents the recrystallization of β-Li_3PS_4 or Li_3PS_4·solvent complexes. The fact that i-PrOH does not dissolve β-Li_3PS_4 completely might also show that not only the OH or NH bonds, respectively, play an important role in the dissolution process but also the size of the solvent molecules. Due to the size of *i*-PrOH, the nucleophilic substitution reaction can be expected to be sterically hindered.[15] Additionally, the polarity could play a role since NMF is much more polar than *i*-PrOH. These correlations are also reflected in the Hansen solubility parameters[48,49] of the considered solvents, which are summarized in Table S2. A strong interrelationship of the polar and hydrogen-bonding cohesion parameters δ_P and δ_H and the

https://doi.org/10.1021/acsaem.2c03278
ACS Appl. Energy Mater. 2023, 6, 7790−7802

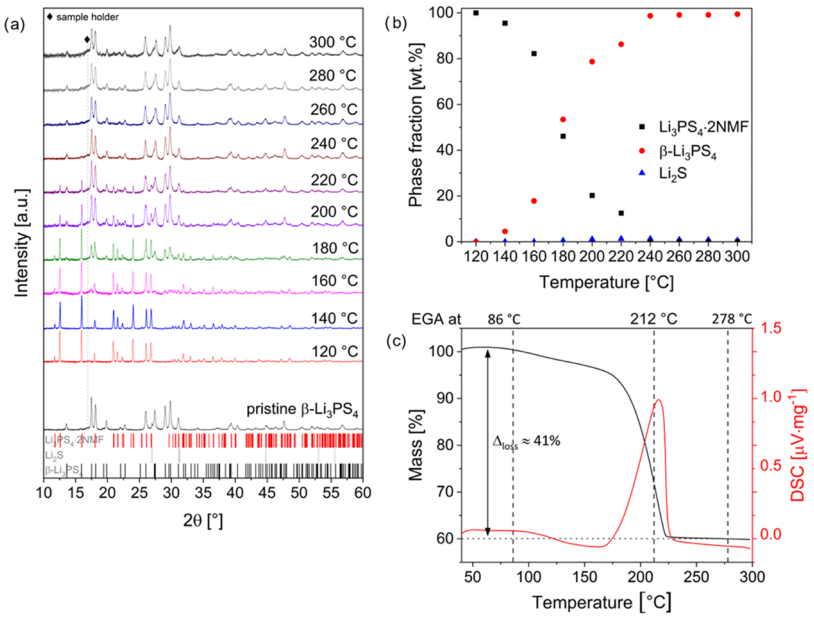

Figure 2. X-ray diffraction patterns (a) and quantitative phase analysis (b) of reheated samples in comparison to pristine β-Li_3PS_4 and Li_3PS_4·2NMF obtained after the treatment of β-Li_3PS_4 in NMF and after excess solvent removal at 120 °C. The samples were reheated to temperatures between 140 and 240 °C for 4 h at reduced pressures. The decrease/increase of Li_3PS_4·2NMF/β-Li_3PS_4 upon heating to higher temperatures can be followed in (a) by comparing the diffraction pattern of the sample obtained after solvent removal at 120 °C (nearly phase-pure Li_3PS_4·2NMF) with the pattern obtained after reheating to 240 °C (nearly phase-pure β-Li_3PS_4). At lower temperatures, phase mixtures of Li_3PS_4·2NMF and β-Li_3PS_4 are present and therefore the diffraction patterns are superimposed. The positions of the characteristic reflection ticks of β-Li_3PS_4 and Li_2S are again given in black and gray, respectively. The ticks of Li_3PS_4·2NMF are presented in red. (c) TG analysis of Li_3PS_4·2NMF obtained after solvent removal at 120 °C. The sample was continuously heated at a rate of 10 K min^{-1}. EG analysis was performed at 86, 212, and 278 °C to investigate which gases are released during the TG analysis. These results are given in Figure S6.

solubility as well as observed degree of decomposition seems to be present.

Nonpolar and aprotic solvents, on the other hand, cannot break the bonding between the Li^+ cations and PS_4^{3-} anions. Consequently, this does not lead to a complete dissolution but to the formation of suspensions. From these, β-Li_3PS_4 can be recovered after the removal of the solvent; however, they do not have a significantly high solubility for solvating a considerable amount of β-Li_3PS_4. It should be emphasized that solubility limits $\ll$ 5 g/L as observed for the nonpolar and aprotic solvents diminish the economic viability and efficiency of possible recycling approaches based on the dissolution of the electrolyte strongly. Therefore, they are not further considered in this work. Still, they might become interesting for other recycling strategies in which the solvent should influence the electrolyte as little as possible (e.g., for separation processes based on physical separation or froth floatation).

3.2. Dissolution of β-Li_3PS_4 in NMF and Its Recrystallization Mechanism. A complete dissolution of β-Li_3PS_4 in NMF is already observed when using a molar ratio of ~1:14 of β-Li_3PS_4 to NMF, which corresponds to an approximate solid-to-liquid ratio of 200 mg/1 mL. For this highest concentration, the obtained clear solution (Figure S3) has a bright yellow color and is highly viscous. Lower relative amounts of NMF cannot fully dissolve β-Li_3PS_4, and a cloudy suspension is formed. An increase in the amount of NMF by a factor of ~4 leads, on the other hand, to a significant decrease in the viscosity of the obtained solution (Figure S4). With this, the time needed for the dissolution also drops considerably from ~ 2 h to 2 to 3 min. This lower viscosity is important when considering that in a recycling process, a separation of the electrode materials from the electrolyte solution should be performed using filtration or centrifugation.

The boiling point of NMF has been reported to be between 180 and 200 °C.[50,51] As described in Section 3.1, when using a lower evaporation temperature of 120 °C, the removal of excess NMF from the solution results in the formation of a white powder with an X-ray powder diffraction pattern significantly different from β-Li_3PS_4 (Figure 2a) for which the crystal structure has not been reported previously. This phase can, however, be transformed into β-Li_3PS_4 after additional heat treatments. For this, the sample was heated to various temperatures between 140 and 300 °C (Figure 2a). A quantitative phase analysis (Figure 2b) reveals that temperatures significantly above the boiling point of NMF are required to recrystallize β-Li_3PS_4, suggesting that a certain driving force is required to transform the intermediate phase to β-Li_3PS_4. Therefore, it can be assumed that this intermediate phase is a Li_3PS_4·xNMF complex phase as also observed when using other solvents like, for example, ACN[12] or DME.[5] Only after heating to temperatures of $\geq$ 240 °C, phase-pure samples are obtained, whereas for all other temperatures, phase mixtures of the unknown phase and β-Li_3PS_4 are found. When comparing the XRD patterns of the pristine and the recrystallized β-Li_3PS_4, no significant differences in reflex intensity ratios are found. Rietveld analysis of the sample obtained after heating to 240 °C indicates a small change of lattice parameters for the pristine and recrystallized β-Li_3PS_4 ($a_{pristine}$ = 12.9959(4) Å, $b_{pristine}$ = 8.0504(3) Å, $c_{pristine}$ = 6.1430(2) Å vs $a_{recrystallized}$ = 12.9564(5) Å, $b_{recrystallized}$ = 8.0961(3) Å, $c_{recrystallized}$ = 6.1428(2) Å). The cell volume of the recrystallized β-Li_3PS_4 is bigger by only 0.26%, suggesting only minimal structural changes (e.g., difference in defect concentrations). Additionally, an increase of the

https://doi.org/10.1021/acsaem.2c03278
ACS Appl. Energy Mater. 2023, 6, 7790−7802

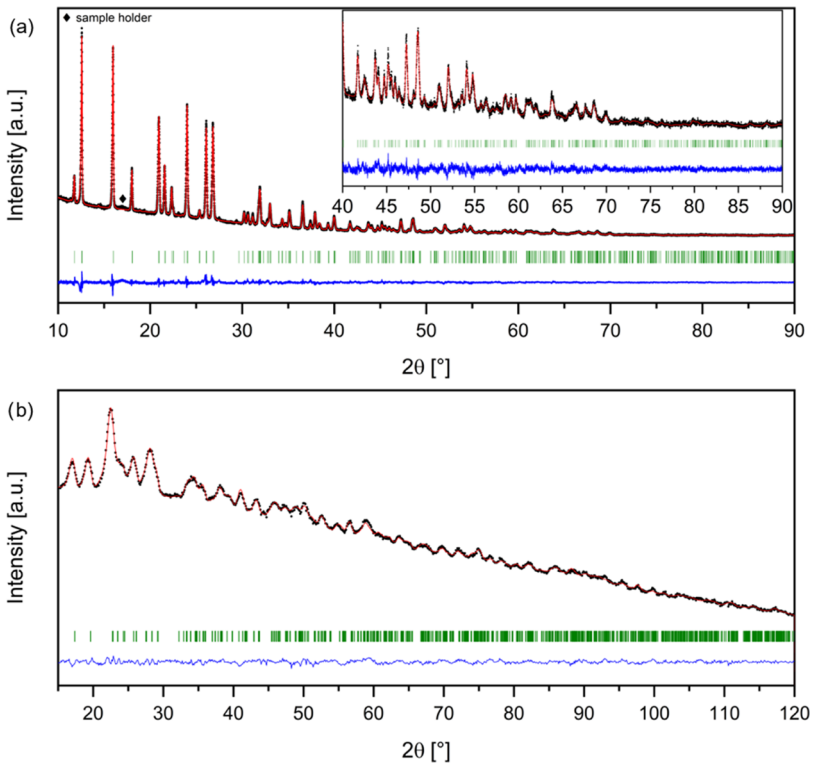

Figure 3. Rietveld refinements of X-ray (a) and neutron (b) diffraction data of Li_3PS_4·2NMF with the model obtained using the rigid body method and simulated annealing. The inset in (a) shows a magnification of the angular range between 40 and 90°. The comparably low signal-to-noise ratio of the neutron diffraction data is due to the incoherent scattering of the hydrogen atoms.

Table 1. Structural Parameters of Li_3PS_4·2NMF (Space Group: *C*2/*c*) as Obtained from Rietveld Analysis Using the Rigid Body Method and Simulated Annealing

atom	Wyckoff position		*x*	*y*	*z*	occupancy	*B* [Å^2]
Li1	4*e*		0	0.339(3)	3/4	1	4.0(5)
Li2	8*f*		0.820(1)	0.196(3)	0.059(1)	1	9.4(6)
P1	4*e*		0	0.8516(6)	3/4	1	3.1(1)
S1	8*f*		0.8801(2)	0.0472(3)	0.7083(2)	1	3.1(1)
S2	8*f*		0.0137(2)	0.6457(3)	0.8528(1)	1	3.8(1)
C1	8*f*		0.6128(5)	0.747(1)	0.0228(4)	1	4.8(1)
C2	8*f*		0.691(4)	0.422(5)	0.105(2)	1	4.8(1)
H1	8*f*		0.704(8)	0.328(8)	0.160(3)	1	4.7(3)
H2	8*f*		0.619(2)	0.620(3)	0.136(3)	1	4.7(3)
H3	8*f*		0.663(5)	0.72(1)	0.006(5)	1	20.4(8)
H4	8*f*		0.619(7)	0.899(6)	0.045(2)	1	20.4(8)
H5	8*f*		0.556(4)	0.734(9)	0.965(3)	1	20.4(8)
N1	8*f*		0.634(2)	0.598(3)	0.095(1)	1	4.8(1)
O1	8*f*		0.722(4)	0.368(7)	0.055(2)	1	4.8(1)
a [Å]	15.8943(4)	*b* [Å]	6.0274(2)	*c* [Å]	16.9540(4)	*β* [°]	117.747(2)
R_{wp} (XRD + NPD) [%]		1.26	GOF(XRD + NPD)		1.09	R_{Bragg} [%]	1.69 (XRD)
							0.25 (NPD)

amorphous phase fraction from ∼ 8 wt % in the pristine sample to ∼ 35 wt % in the recrystallized sample was determined using the internal standard method (Figure S5), indicating that the heating temperature of 240 °C is not high enough and/or the duration of 4 h not long enough to obtain a complete recrystallization. When using higher heating temperatures, the amorphous phase fractions still remain significantly higher compared to the pristine sample. However, it has been shown that higher crystallinity does not lead to improved functional properties such as ionic conductivity and that a suppression of crystallization might be beneficial as long as the solvent can be removed completely.[52,53]

To understand the changes observed upon recrystallization of *β*-Li_3PS_4 from the intermediate phase and the overall recrystallization mechanism better, the intermediate phase was investigated in more detail and its crystal structure was determined. Indexing of the XRD pattern (Figure 3a) indicated the formation of a C-centered monoclinic phase with lattice parameters of $a \approx 15.89$ Å, $b \approx 6.02$ Å, $c \approx 16.95$ Å, and $\beta \approx 117.75°$. A weight loss of ∼41% in TG analysis (Figure 2c) shows further that this phase contains approximately 2 NMF

https://doi.org/10.1021/acsaem.2c03278
ACS Appl. Energy Mater. 2023, 6, 7790−7802

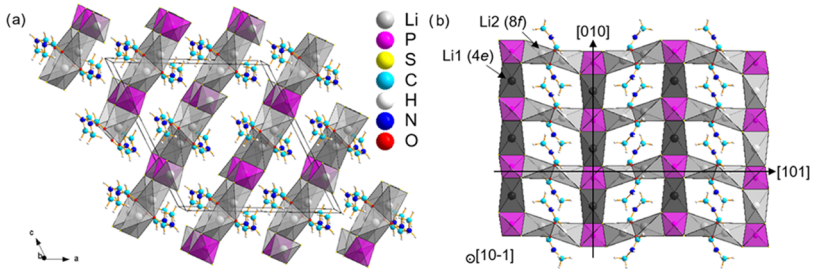

Figure 4. Crystal structure of Li_3PS_4·2NMF (a) and top view onto one of the Li_3PS_4·2NMF layers (b) as obtained from Rietveld analysis using the rigid body method and simulated annealing.

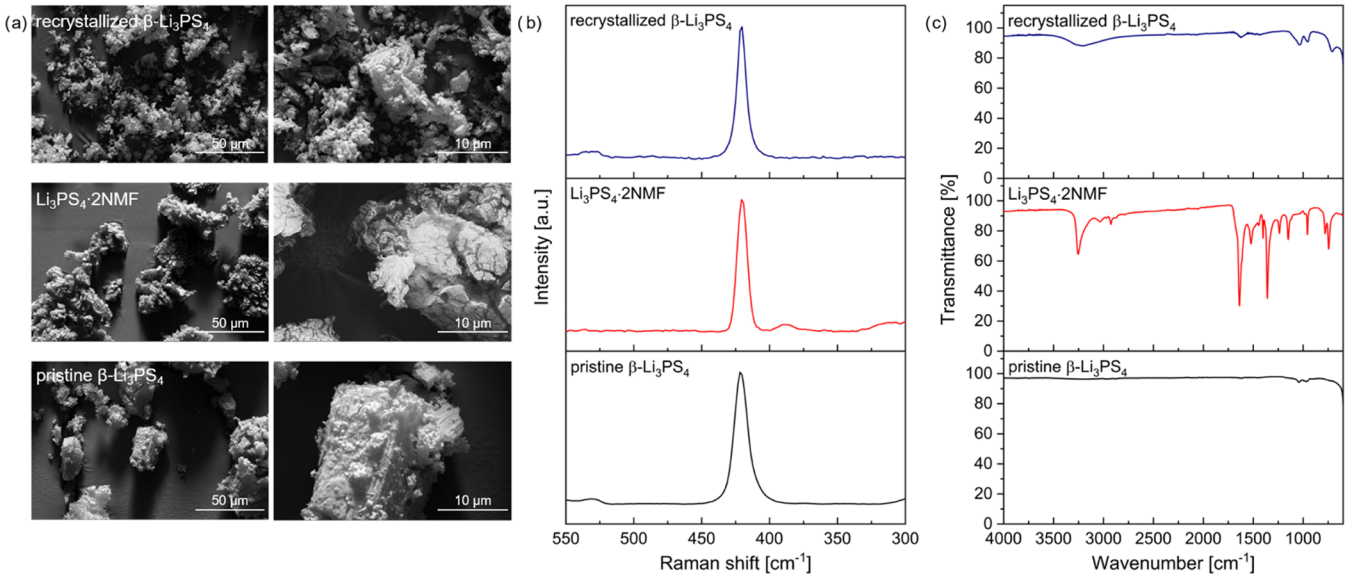

Figure 5. Comparison of scanning electron micrographs (a), Raman spectra (b), and FTIR spectra (c) of pristine β-Li_3PS_4, Li_3PS_4·2NMF, and recrystallized β-Li_3PS_4.

molecules per Li_3PS_4 unit, suggesting the formation of a complex with composition Li_3PS_4·2NMF. Taking space requirements of Li_3PS_4[54,55] and NMF[51,56] into consideration, it can be concluded that the cell is likely to contain 4 formula units per unit cell. Evolving gas analysis (Figure S6) confirms that the mass loss is due to the release of NMF from the crystal structure. The comparatively constant mass at temperatures >225 °C confirms that the release of NMF is complete at this temperature, which justifies the choice of a recrystallization temperature of 240 °C. Additional TG measurements with isothermal holding steps (Figure S7) suggest that accelerating decomposition of the recrystallized phases takes place when heating to higher temperatures.

Ab initio structural solution was attempted using the rigid body method in combination with simulated annealing within different *C*-centered monoclinic structures (e.g., *C*2/*m* and *C*2/*c*). For this, rigid bodies of PS_4 units (as also indicated by Raman spectroscopy) as well as molecular NMF units were defined based on reported bond lengths and bond angles.[51,54−56] Reasonable flexibility in these parameters was given. Translation, rotation, and torsion angles were refined to identify the relative orientations of the different building units. Structural solutions in *C*2/*m* do not result in a reasonable relative orientation of PS_4 units with sufficient quality of the fits. In contrast, structural solutions in *C*2/*c* resulted in a plausible orientation of PS_4 and NMF units toward each other, in agreement with the observed systematic extinctions.

By coupling additional neutron diffraction data (Figure 3b) to the X-ray diffraction data (Figure 3a), plausible approximate positions of the Li ions could be identified, which are located on two different crystallographic sites (4*e* and 8*f*). The corresponding structural parameters after refining the positional and thermal parameters within a Rietveld analysis are given in Table 1. The obtained high thermal parameters of the H ions of the methyl group (H3−H5) indicate a partial disorder in that region of the structure, most likely explained by the rotational degree of freedom of the methyl group. The crystal structure is represented in Figure 4.

Additional *ab initio* DFT simulations confirm the validity of the determined structure. The DFT-optimized structural parameters are given in Table S3 for comparison. Most interestingly, they confirm the orientation of the methyl group as well as positioning of the Li2 atom toward the oxygen group of the NMF molecule.

The structure consists of shifted layers of composition Li_3PS_4·2NMF stacked along the $[1\bar{0}1]$ direction. Two different interactions of the molecular species and Li_3PS_4 can be identified: The oxygen ions are coordinated to the Li ions on the 8*f* site and the NH groups have a weak interaction with the nearest PS_4 units in the adjacent layers. This results in strong ionic interactions within the layers and weaker dipole interactions perpendicular to them. The latter interaction is also reflected in a change of the NH stretching vibration IR mode (Figure 5c). This is also important considering the

https://doi.org/10.1021/acsaem.2c03278
ACS Appl. Energy Mater. 2023, 6, 7790−7802

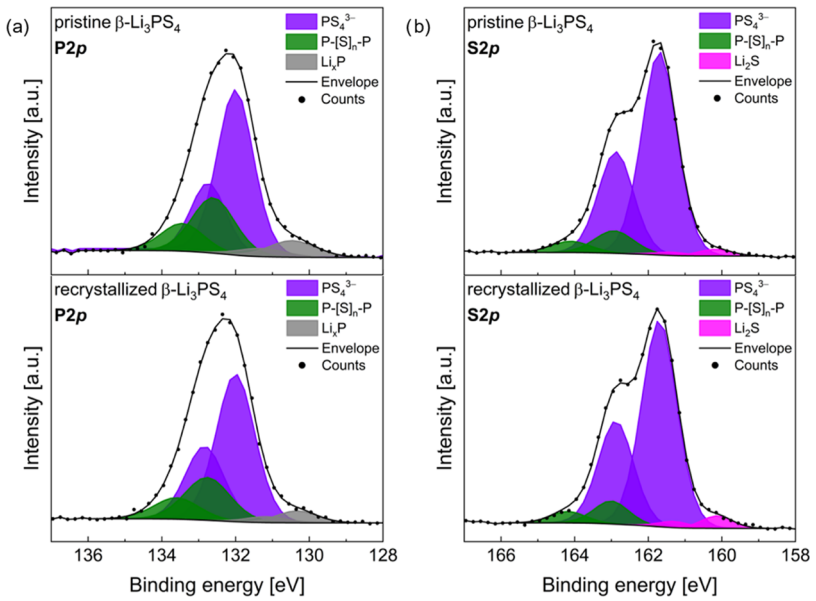

Figure 6. Comparison between P 2p (a) and S 2p (b) XPS spectra of pristine and recrystallized β-Li_3PS_4.

solution mechanism and confirms the role of the NH bonds for stabilizing the PS_4^{3-} units in solution.

Since the Li ions on the 8*f* site are connected to both PS_4 tetrahedra and NMF molecules, this results in chains according to $\cdots S_2LiO_2LiS_2PS_2LiO_2LiS_2\cdots$ along the [101] direction. The Li ion on the 4*e* site is located in a tetrahedral LiS_4 polyhedron between two PS_4 tetrahedra. This results in chains according to $\cdots S_2LiS_2PS_2LiS_2\cdots$ along the crystallographic *b* direction. This interconnectivity of tetrahedra is also highlighted in Figure 4b.

It becomes also evident that potential interstitial sites within and between Li_3PS_4·2NMF layers are in close distance to the nonpolar methyl groups of the NMF molecules. Therefore, their occupation by ionic species such as Li^+ becomes less likely due to mainly nonionic weak van der Waals forces around them.

When comparing the structure of Li_3PS_4·2NMF to Li_3PS_4·DME[5] and Li_3PS_4·ACN,[12] significant differences can be found. The latter two compounds crystallize in the tetragonal crystal system and consist of alternating layers of $Li_2PS_4^-$ separated by layers with the composition of $(solv)_nLi^+$. In contrast to Li_3PS_4·2NMF, these two structures are more similar to the structure of β-Li_3PS_4 also consisting of $Li_2PS_4^-$ layers separated by Li^+ layers. As the structural transition to the complex can be considered as a topotactic solvent insertion under volume increase, a complete dissolution of β-Li_3PS_4 in DME or ACN is not possible.

Morphological and structural changes of these samples were additionally investigated using a combination of scanning electron microscopy and Raman, infrared, as well as X-ray photoelectron spectroscopy (Figures 5 and 6). The morphologies of pristine β-Li_3PS_4 and Li_3PS_4·2NMF are similar with respect to the particle size; however, the particle shapes differ. Li_3PS_4·2NMF particles appear to have considerably more and deeper cracks throughout the particle surfaces compared to β-Li_3PS_4. This agrees with the weak dipolar interactions between the layers of Li_3PS_4·2NMF (Figure 4), resulting in a comparatively easy splitting between different parts of a particle. Recrystallized β-Li_3PS_4 consists of particles with a wider particle size distribution with overall smaller particles. This is probably related to the outgassing of NMF in a random fashion from the crystal structure, resulting in stress fractions of the particles and the formation of grain boundaries.

A comparison between the Raman and FTIR spectra of pristine β-Li_3PS_4, Li_3PS_4·2NMF, and recrystallized β-Li_3PS_4 gives further insights into structural changes. Raman spectroscopy (Figure 5b) confirms that all samples contain ortho-thiophosphate units indicated by the signal at ~421 cm^{-1}.[46,47] Other thiophosphate species cannot be observed, neither during the dissolution process (Figure S8a) nor in Li_3PS_4·2NMF or the recrystallized β-Li_3PS_4 after the removal of NMF. The PS_4^{3-} units are also preserved in solution. For Li_3PS_4·2NMF, less pronounced signals are additionally found at ~315 and 388 cm^{-1}, which can be assigned to the NMF within the structure.[9] The most significant differences in the FTIR spectra (Figure 5c) can be again ascribed to the presence of NMF in the samples. A comparison of the spectra of pure NMF, β-Li_3PS_4 dissolved in NMF and Li_3PS_4·2NMF (Figure S8a) reveals that the observed signals correspond to vibrations of NMF which agrees with previously reported spectra of NMF.[57,58] This is also supported by the fact that the spectrum of pristine β-Li_3PS_4 features no strong signals. Characteristic shifts of NMF vibration modes can be observed for Li_3PS_4·2NMF. As already mentioned, the strongest shift is observed for the NH stretching vibration mode in the range between 3100 and 3480 cm^{-1}, which can be attributed to the interactions between NH groups of NMF molecules and PS_4^{3-} units in the layered structure of Li_3PS_4·2NMF.[58] Other modes (e.g., the CH_3 symmetric bend at ~1375 cm^{-1}) show less pronounced shifts since weaker interactions take place. Similar trends in band shifting are observed in the Raman spectra. The NMF-related signals in the FTIR spectrum of the recrystallized β-Li_3PS_4 decrease significantly in number and relative intensity compared to the spectrum of Li_3PS_4·2NMF (or to the spectra of pure NMF and β-Li_3PS_4 dissolved in NMF (Figure S8a)). The observed signals are relatively broad, and it is difficult to assign them to specific vibration modes; however, NH stretching (3400−3100 cm^{-1}), CH and $(CH_3)N$ stretching (2900−2800 cm^{-1}), C═O stretching (1700−1650 cm^{-1}), and CH and CH_3 bending (1550−1400 cm^{-1}) vibrations might be present.[57,58] This suggests that NMF might have partially decomposed during the evaporation process. Such NMF fragments are likely to influence the chemical nature of the recrystallized sample and probably contribute to the increased

https://doi.org/10.1021/acsaem.2c03278
ACS Appl. Energy Mater. 2023, 6, 7790−7802

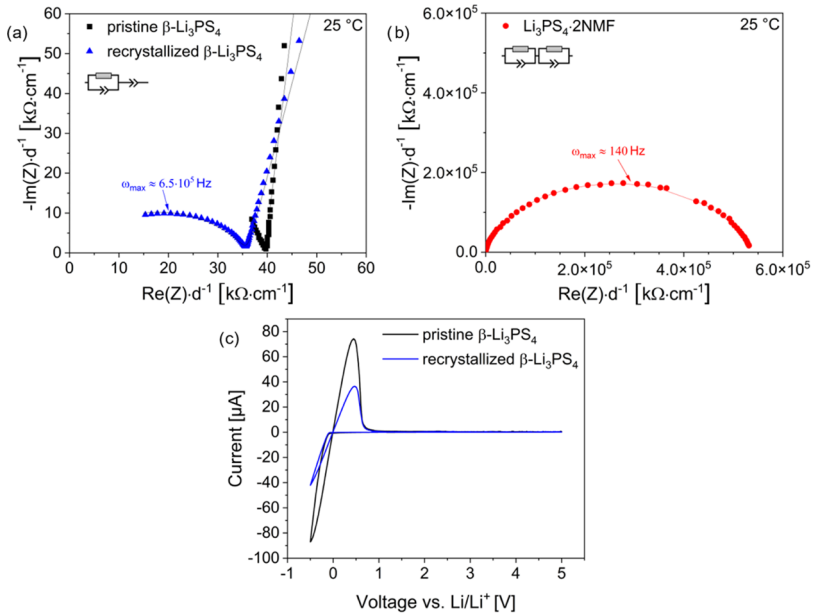

Figure 7. Nyquist plots of pristine and recrystallized β-Li_3PS_4 (a) and Li_3PS_4·2NMF (b) measured at 25 °C with corresponding fits. Cyclic voltammograms of the Li|β-Li_3PS_4|stainless steel cells containing pristine and recrystallized β-Li_3PS_4 (scan rate: 5 mV s^{-1}) (c).

amount of the amorphous phase(s). The absence of intact NMF molecules after drying is also in accordance with the performed TG and EG analysis, which shows that NMF is released at temperatures < 240 °C. In addition, the spectra of pristine and recrystallized β-Li_3PS_4 feature two signals at ∼1042 and 961 cm^{-1}, which could indicate the formation of small amounts of $PS_{4-x}O_x^{3-}$ groups.[59] However, there is no indication for such $PS_{4-x}O_x^{3-}$ species in Raman spectroscopy[60,61] and XRD (at least not in the form of crystalline phases). This also illustrates that special attention has to be paid to the amorphous phase fraction present in the sample. Its detailed nature could be influenced by two factors: (1) The release of solvent molecules and the subsequent crystallization process can result in a different short-range structural arrangement within the obtained amorphous phase compared to, for example, mechanochemical synthesis approaches. (2) Additional subtle changes in the chemical composition (e.g., from small degrees of decomposition of the solvent phase) might further affect the detailed short-range structure. Both can result in different amounts of defects or structural pathways for the lithium-ion transport and could therefore have a significant influence on the properties of the samples.

Since the XRD analysis, Raman, and FTIR spectroscopy do not show considerable structural changes between pristine and recrystallized β-Li_3PS_4, XPS measurements were additionally carried out. The comparison between the P 2p and S 2p spectra of the pristine and recrystallized β-Li_3PS_4 is shown in Figure 6. The main signal corresponds to the P−S bond in the PS_4^{3-} units of β-Li_3PS_4 at 132.0 eV (P 2p) and 161.7 eV (S 2p).[62−64] The low-intensity signals at lower binding energies than the PS_4^{3-} peaks can be assigned to reduced phosphorous species Li_xP ($0 < x < 3$) and Li_2S in the P 2p and S 2p spectra, respectively.[63,65] The latter agrees with the Li_2S impurity phase observed in the XRD measurements. The presence of P−$[S]_n$−P type bonds is indicated from the doublet at ∼163.0 and 164.2 eV in the S 2p spectrum.[65] An unambiguous assignment of the signal found at higher binding energies in the P 2p spectrum is not possible since P−$[S]_n$−P as well as oxygenated phosphorous species (phosphates, metaphosphates, or $PS_{4-x}O_x^{3-}$)[32,66] can be present at these binding energies impeding the deconvolution. For the recrystallized β-Li_3PS_4, a small shift to higher energies as well as a small increase in the concentration of this signal is found. This indicates that oxygenated phosphorous species, possessing higher binding energies than P−$[S]_n$−P,[67,68] might have formed to a minor extent in addition to P−$[S]_n$−P. Most likely, these species can be assigned to the amorphous phase fraction since additional reflections are absent in the diffraction data. Besides this, an increase in the intensity of carbonate-related signals in the C 1s and O 1s spectra is observed in the recrystallized sample compared to the pristine sample. Nevertheless, no significant changes are observed, suggesting minor degradation of the recrystallized β-Li_3PS_4 in comparison to the pristine β-Li_3PS_4 after the solvent treatment.

To investigate the influence of the solvent treatment on the ionic conductivity, impedance measurements were performed on pristine β-Li_3PS_4, Li_3PS_4·2NMF and recrystallized β-Li_3PS_4. The Nyquist plot of the pristine and recrystallized β-Li_3PS_4 (measured at 25 °C) is shown in Figure 7a. Both samples show at first glance a similar behavior with a half semicircle and an x-axis intercept at high frequencies and a mid- and low-frequency tail. The Bode plots (Figure S10) indicate that a single Li-conducting phenomenon is dominant. It was found that a single, parallel R/CPE element (R = resistor, CPE = constant phase element) connected in series to a CPE can be used for fitting the Li-ion transport process and electrode-ion-blocking effect at the electrode, respectively. From the fits, the RT conductivity values of pristine and recrystallized β-Li_3PS_4 were determined to be 2.3 × 10^{-5} and 2.2·10^{-5} S cm^{-1} at 25 °C, respectively, which is the same within experimental error.[69] The capacitance values for the pristine and recrystallized β-Li_3PS_4 are 4 × 10^{-11} vs 8 × 10^{-11} F (relative dielectric constants ε_r 14 vs 70), respectively, which are slightly different, though in the same order of magnitude. Minor impacts of the measurement conditions (see also comparison to samples measured without an applied pressure shown in Figure S9) can be observed. It is known that the existence of amorphous phases and regions of low crystallinity as found in the

https://doi.org/10.1021/acsaem.2c03278
ACS Appl. Energy Mater. 2023, 6, 7790−7802

recrystallized sample can have a complex influence on the conductivity, which can be even beneficial within certain ranges.[52,53,70] The asymmetry observed in the Bode plot of the recrystallized sample (Figure S10) suggests such a more complex conduction behavior beyond a single transport process. However, due to similar time constants, these processes cannot be well deconvoluted from each other and thus do not allow for a more detailed characterization. Nevertheless, it can be concluded that the presented procedure serves to recover the electrolyte in a conductive state similar to the pristine samples.

Li_3PS_4·2NMF shows a completely different response in the impedance measurements. From the Nyquist plot (Figure 7b), only a single semicircle could be observed within the high- and mid-frequency range along with a low-frequency intercept on the *x*-axis and no blocking tail, which indicates that this phase is considerably less Li-ion-conducting with an insufficient conductivity for an application within a solid-state battery. This can further be confirmed from the Bode plots (Figure S10), where at low frequencies the phase angle is found to be closer to 0°, indicating a resistive instead of a capacitive behavior. To obtain a good estimate of the overall resistance, two R/CPE elements had to be used in series since a single R/CPE element could not fit the data sufficiently well due to the strong depression of the semicircle observed in the spectrum. For the model with two R/CPE elements, the individual elements have similar capacitances (5×10^{-11} F vs 4×10^{-11} F at RT), relative dielectric constants ε_r (42 vs 34), and resistances (~30 vs ~10 MOhm at RT) and cannot be well separated; thus, only a single maximum frequency is indicated in Figure 7b. The corresponding capacitances are in a similar order of magnitude and indicate the dominance of the bulk conduction processes on the resistivity of the compound. A conductivity value of 1.7×10^{-9} S·cm^{-1} at 25 °C was calculated, which is 4 orders of magnitude lower than that of the pristine and the recrystallized β-Li_3PS_4. This decreased ion conductivity is expected with respect to the crystal structure of Li_3PS_4·2NMF since there are no continuous pathways for Li-ion conduction, and due to strong ionic interactions between lithium ions and the oxygen ions of the solvent molecules. Additionally, it should be emphasized that the amorphous phase fraction within this sample is 49.1 wt % (Figure S5), and thus significantly higher compared to the pristine and recrystallized β-Li_3PS_4. The presence of poorly conducting Li_3PS_4·2NMF within the sample could severely influence the overall conductivity according to percolation theory depending on the relative phase fractions and their spatial distribution.

Thus, large amounts of remaining Li_3PS_4·2NMF could have a detrimental impact on the conductivity of recrystallized samples after solvent treatment in a possible recycling application, making it essential to optimize the solvent removal procedure. At the same time, the found amorphous phase(s) (i.e., their composition (including effects due to solvent decomposition), structure, volume fraction, and three-dimensional (3D) structure in relation to other phases) could influence the conductivity further. With respect to this, further systematic studies are necessary.

To investigate the influences of the dissolution and recrystallization on the electrochemical stability of the recrystallized β-Li_3PS_4, cyclic voltammetry was conducted using Li|β-Li_3PS_4|stainless steel cells. The cyclic voltammograms of the cells containing the pristine and recrystallized β-Li_3PS_4 are shown in Figure 7c. For both electrolytes, comparable behavior is observed. During the first cathodic sweep starting from the OCVs of the cells, a reduction current is observed starting at ca. −0.1 V. In the subsequent anodic sweep, an anodic current is measured up to voltages of ~1 V. These peaks can be related to lithium deposition and removal.[3] Besides these signals, no significant currents are observed in the scanned potential range indicating a good electrochemical stability of the investigated electrolytes against Li.

4. CONCLUSIONS

The study shown here highlights the importance of separating solvent-based synthesis from dissolution and recrystallization strategies of β-Li_3PS_4. Though many solvents have been reported to be suitable for the synthesis of β-Li_3PS_4, recrystallization requires the use of polar, weakly protic solvents such as NMF. The recrystallization proceeds via the intermediate phase Li_3PS_4·2NMF, which can be removed using an optimized heating process. This step is necessary in order to obtain conductivities of the recrystallized β-Li_3PS_4 comparable to the pristine material.

We emphasize that the increase in amorphous phase has to be regarded as critical for the use of a recrystallization procedure within a recycling process. Though it leads to comparable room-temperature conductivities, it is so far not clear to what extent repeated dissolution and recrystallization might impact the functional electrolyte properties, which will be decisive to establish these materials within a circular economy. It should also be acknowledged that further systematic studies on the influence of the crystallinity of the recrystallized electrolyte which can be likely adjusted using appropriate heating parameters would be of importance. Here, a special focus should be set on the investigation of the detailed nature of the amorphous phase fraction using, e.g., pair distribution function analysis and NMR spectroscopy.

Furthermore, for a more holistic view on the recycling of solid-state batteries, the role of the electrode materials within the electrode composites needs to be considered. This might demonstrate the necessity to adapt the recrystallization process to the electrode materials used. This will be reported in a follow-up article.

■ ASSOCIATED CONTENT

Supporting Information

The Supporting Information is available free of charge at https://pubs.acs.org/doi/10.1021/acsaem.2c03278.

Physical and chemical properties of the solvents used; Rietveld refinements of complexes Li_3PS_4·DME, Li_3PS_4·ACN, and complexes Li_3PS_4·2NMF; X-ray diffraction patterns of precipitates after solvent treatment of β-Li_3PS_4 in *i*-PrOH, EtOH, and MeOH after additional heat treatment at 550 °C; Hansen solubility parameters of the solvents used; photograph of β-Li_3PS_4 in NMF using different molar or liquid-to-solid ratios of β-Li_3PS_4 to NMF; shear stress and viscosity as a function of the shear rate of β-Li_3PS_4 in NMF with a solid-to-liquid ratio; Rietveld refinements of pristine β-Li_3PS_4, Li_3PS_4·2NMF, and recrystallized β-Li_3PS_4 heated to 240, 260, 280, and 300 °C mixed with 50 wt % Al_2O_3, evolving gas analysis; TG analysis of Li_3PS_4·2NMF with isothermal holding steps; structural parameters of Li_3PS_4·2NMF optimized in DFT simulation; Raman and FTIR spectra of NMF; β-Li_3PS_4 dissolved in an excess of NMF and Li_3PS_4·2NMF; Nyquist plots of pristine and recrystallized β-Li_3PS_4

https://doi.org/10.1021/acsaem.2c03278
ACS Appl. Energy Mater. 2023, 6, 7790−7802

measured at 25 °C without an applied pressure with corresponding fits and Arrhenius plots; and Bode plots of pristine β-Li_3PS_4, Li_3PS_4·2NMF, and recrystallized β-Li_3PS_4 (PDF)

Li_3PS_4·2NMF (CIF)

AUTHOR INFORMATION

Corresponding Author

Kerstin Wissel − *Institute for Materials Science, Materials Analysis, Technical University of Darmstadt, 64287 Darmstadt, Germany;* orcid.org/0000-0003-4418-0595; Email: kerstin.wissel@tu-darmstadt.de; Fax: +49 6151 16-21991

Authors

Luise M. Riegger − *Institute for Physical Chemistry, Justus-Liebig-University Gießen, 35392 Gießen, Germany; Center for Materials Research (ZfM), Justus-Liebig-University Gießen, 35392 Gießen, Germany*

Christian Schneider − *Max Planck Institute for Solid State Research, 70569 Stuttgart, Germany*

Aamir I. Waidha − *Institute for Materials Science, Materials Analysis, Technical University of Darmstadt, 64287 Darmstadt, Germany*

Theodosios Famprikis − *Department of Radiation Science and Technology, Delft University of Technology, Delft 2629JB, The Netherlands;* orcid.org/0000-0002-7946-1445

Yuji Ikeda − *Institute for Materials Science, Materials Design, University of Stuttgart, 70569 Stuttgart, Germany;* orcid.org/0000-0001-9176-3270

Blazej Grabowski − *Institute for Materials Science, Materials Design, University of Stuttgart, 70569 Stuttgart, Germany;* orcid.org/0000-0003-4281-5665

Robert E. Dinnebier − *Max Planck Institute for Solid State Research, 70569 Stuttgart, Germany*

Bettina V. Lotsch − *Max Planck Institute for Solid State Research, 70569 Stuttgart, Germany; Department of Chemistry, Ludwig-Maximilians-Universität München, 81377 München, Germany;* orcid.org/0000-0002-3094-303X

Jürgen Janek − *Institute for Physical Chemistry, Justus-Liebig-University Gießen, 35392 Gießen, Germany; Center for Materials Research (ZfM), Justus-Liebig-University Gießen, 35392 Gießen, Germany;* orcid.org/0000-0002-9221-4756

Wolfgang Ensinger − *Institute for Materials Science, Materials Analysis, Technical University of Darmstadt, 64287 Darmstadt, Germany*

Oliver Clemens − *Institute for Materials Science, Chemical Materials Synthesis, University of Stuttgart, 70569 Stuttgart, Germany;* orcid.org/0000-0002-0860-0911

Complete contact information is available at: https://pubs.acs.org/10.1021/acsaem.2c03278

Author Contributions

K.W., W.E., and O.C. conceived and designed the study. K.W. prepared the samples and measured and analyzed the XRD, SEM, Raman, and FTIR spectroscopy data. L.M.R. measured and analyzed the XPS data. K.W. and L.M.R. performed the EIS and interpreted the data together with A.I.W. under the guidance of J.J. T.F. measured neutron diffraction. C.S. measured and analyzed TGA and EGA under the guidance of B.V.L. Y.I. performed the DFT calculations under the guidance of B.G. R.E.D. helped with the analysis of diffraction data. K.W. wrote the manuscript. All authors discussed and revised the work.

Notes

The authors declare no competing financial interest.

ACKNOWLEDGMENTS

This work was funded by German federal state of Hessen (Hessen Agentur, HA-Project Number 848/20-08). L.M.R. and J.J. acknowledge the financial support by the German Federal Ministry of Research and Education (BMBF), projects 03XP0433D and 03XP0430A (FestBatt). C.S. and B.V.L. acknowledge financial support by the German Federal Ministry of Research and Education (BMBF), projects 03XP0177B (FestBatt), and the Deutsche Forschungsgemeinschaft via the Cluster of Excellence e-conversion (EXC2089). Y.I. and B.G. acknowledge the funding from the European Research Council (ERC) under the European Union's Horizon 2020 research and innovation programme (grant agreement no. 865855), the support by the Stuttgart Center for Simulation Science (SimTech), and the support by the state of Baden-Württemberg through bwHPC and the German Research Foundation (DFG) through grant no. INST 40/575-1 FUGG (JUSTUS 2 cluster). K.W. thanks Stephan Pflumm, Dr. Klaus Dirnberger, and Prof. Dr. Sabine Ludwigs for their help in the viscosity measurements.

REFERENCES

(1) Zhang, Q.; Cao, D.; Ma, Y.; Natan, A.; Aurora, P.; Zhu, H. Sulfide-Based Solid-State Electrolytes: Synthesis, Stability, and Potential for All-Solid-State Batteries. *Adv. Mater.* **2019**, *31*, No. 1901131.

(2) Wang, H.; Hood, Z. D.; Xia, Y.; Liang, C. Fabrication of ultrathin solid electrolyte membranes of β-Li_3PS_4 nanoflakes by evaporation-induced self-assembly for all-solid-state batteries. *J. Mater. Chem. A* **2016**, *4*, 8091−8096.

(3) Lim, H.-D.; Lim, H.-K.; Xing, X.; Lee, B.-S.; Liu, H.; Coaty, C.; Kim, H.; Liu, P. Solid Electrolyte Layers by Solution Deposition. *Adv. Mater. Interfaces* **2018**, *5*, No. 1701328.

(4) Phuc, N. H. H.; Morikawa, K.; Totani, M.; Muto, H.; Matsuda, A. Chemical synthesis of Li_3PS_4 precursor suspension by liquid-phase shaking. *Solid State Ionics* **2016**, *285*, 2−5.

(5) Sedlmaier, S. J.; Indris, S.; Dietrich, C.; Yavuz, M.; Dräger, C.; von Seggern, F.; Sommer, H.; Janek, J. Li_4PS_4I: A Li^+ Superionic Conductor Synthesized by a Solvent-Based Soft Chemistry Approach. *Chem. Mater.* **2017**, *29*, 1830−1835.

(6) Phuc, N. H. H.; Totani, M.; Morikawa, K.; Muto, H.; Matsuda, A. Preparation of Li_3PS_4 solid electrolyte using ethyl acetate as synthetic medium. *Solid State Ionics* **2016**, *288*, 240−243.

(7) Ito, A.; Kimura, T.; Sakuda, A.; Tatsumisago, M.; Hayashi, A. Liquid-phase synthesis of Li_3PS_4 solid electrolyte using ethylenediamine. *J. Sol-Gel Sci. Technol.* **2022**, *101*, 2−7.

(8) Teragawa, S.; Aso, K.; Tadanaga, K.; Hayashi, A.; Tatsumisago, M. Liquid-phase synthesis of a Li_3PS_4 solid electrolyte using N-methylformamide for all-solid-state lithium batteries. *J. Mater. Chem. A* **2014**, *2*, 5095−5099.

(9) Teragawa, S.; Aso, K.; Tadanaga, K.; Hayashi, A.; Tatsumisago, M. Formation of Li_2S-P_2S_5 Solid Electrolyte from N-Methylformamide Solution. *Chem. Lett.* **2013**, *42*, 1435−1437.

(10) Teragawa, S.; Aso, K.; Tadanaga, K.; Hayashi, A.; Tatsumisago, M. Preparation of Li_2S−P_2S_5 solid electrolyte from N-methylformamide solution and application for all-solid-state lithium battery. *J. Power Sources* **2014**, *248*, 939−942.

(11) Liu, Z.; Fu, W.; Payzant, E. A.; Yu, X.; Wu, Z.; Dudney, N. J.; Kiggans, J.; Hong, K.; Rondinone, A. J.; Liang, C. Anomalous High Ionic Conductivity of Nanoporous β-Li_3PS_4. *J. Am. Chem. Soc.* **2013**, *135*, 975−978.

(12) Calpa, M.; Nakajima, H.; Mori, S.; Goto, Y.; Mizuguchi, Y.; Moriyoshi, C.; Kuroiwa, Y.; Rosero-Navarro, N. C.; Miura, A.; Tadanaga, K. Formation Mechanism of β-Li_3PS_4 through Decomposition of Complexes. *Inorg. Chem.* **2021**, *60*, 6964−6970.
(13) Azhari, L.; Bong, S.; Ma, X.; Wang, Y. Recycling for All Solid-State Lithium-Ion Batteries. *Matter* **2020**, *3*, 1845−1861.
(14) Tan, D. H. S.; Xu, P.; Yang, H.; Kim, M.-c.; Nguyen, H.; Wu, E. A.; Doux, J.-M.; Banerjee, A.; Meng, Y. S.; Chen, Z. Sustainable design of fully recyclable all solid-state batteries. *MRS Energy Sustainability* **2020**, *7*, No. 23.
(15) Hatz, A.-K.; Calaminus, R.; Feijoo, J.; Treber, F.; Blahusch, J.; Lenz, T.; Reichel, M.; Karaghiosoff, K.; Vargas-Barbosa, N. M.; Lotsch, B. V. Chemical Stability and Ionic Conductivity of LGPS-Type Solid Electrolyte Tetra-Li_7SiPS_8 after Solvent Treatment. *ACS Appl. Energy Mater.* **2021**, *4*, 9932−9943.
(16) Nam, Y. J.; Cho, S.-J.; Oh, D. Y.; Lim, J.-M.; Kim, S. Y.; Song, J. H.; Lee, Y.-G.; Lee, S.-Y.; Jung, Y. S. Bendable and Thin Sulfide Solid Electrolyte Film: A New Electrolyte Opportunity for Free-Standing and Stackable High-Energy All-Solid-State Lithium-Ion Batteries. *Nano Lett.* **2015**, *15*, 3317−3323.
(17) Lee, K.; Kim, S.; Park, J.; Park, S. H.; Coskun, A.; Jung, D. S.; Cho, W.; Choi, J. W. Selection of Binder and Solvent for Solution-Processed All-Solid-State Battery. *J. Electrochem. Soc.* **2017**, *164*, A2075−A2081.
(18) Sakuda, A.; Kuratani, K.; Yamamoto, M.; Takahashi, M.; Takeuchi, T.; Kobayashi, H. All-Solid-State Battery Electrode Sheets Prepared by a Slurry Coating Process. *J. Electrochem. Soc.* **2017**, *164*, A2474−A2478.
(19) Yamamoto, M.; Terauchi, Y.; Sakuda, A.; Takahashi, M. Slurry mixing for fabricating silicon-composite electrodes in all-solid-state batteries with high areal capacity and cycling stability. *J. Power Sources* **2018**, *402*, 506−512.
(20) Yamamoto, M.; Terauchi, Y.; Sakuda, A.; Takahashi, M. Binder-free sheet-type all-solid-state batteries with enhanced rate capabilities and high energy densities. *Sci. Rep.* **2018**, *8*, No. 1212.
(21) Yamamoto, M.; Takahashi, M.; Terauchi, Y.; Kobayashi, Y.; Ikeda, S.; Sakuda, A. Fabrication of composite positive electrode sheet with high active material content and effect of fabrication pressure for all-solid-state battery. *J. Ceram. Soc. Jpn.* **2017**, *125*, 391−395.
(22) Ito, S.; Fujiki, S.; Yamada, T.; Aihara, Y.; Park, Y.; Kim, T. Y.; Baek, S.-W.; Lee, J.-M.; Doo, S.; Machida, N. A rocking chair type all-solid-state lithium ion battery adopting Li_2O−ZrO_2 coated $LiNi_{0.8}Co_{0.15}Al_{0.05}O_2$ and a sulfide based electrolyte. *J. Power Sources* **2014**, *248*, 943−950.
(23) Hood, Z. D.; Wang, H.; Pandian, A. S.; Peng, R.; Gilroy, K. D.; Chi, M.; Liang, C.; Xia, Y. Fabrication of Sub-Micrometer-Thick Solid Electrolyte Membranes of β-Li_3PS_4 via Tiled Assembly of Nanoscale, Plate-Like Building Blocks. *Adv. Energy Mater.* **2018**, *8*, No. 1800014.
(24) Oh, D. Y.; Kim, D. H.; Jung, S. H.; Han, J.-G.; Choi, N.-S.; Jung, Y. S. Single-step wet-chemical fabrication of sheet-type electrodes from solid-electrolyte precursors for all-solid-state lithium-ion batteries. *J. Mater. Chem. A* **2017**, *5*, 20771−20779.
(25) van Eijck, L.; Cussen, L. D.; Sykora, G. J.; Schooneveld, E. M.; Rhodes, N. J.; van Well, A. A.; Pappas, C. Design and Performance of a Novel Neutron Powder Diffractometer: PEARL at TU Delft. *J. Appl. Crystallogr.* **2016**, *49*, 1398−1401.
(26) Kresse, G.; Furthmüller, J. Efficiency of ab-initio total energy calculations for metals and semiconductors using a plane-wave basis set. *Comput. Mater. Sci.* **1996**, *6*, 15−50.
(27) Kresse, G.; Joubert, D. From ultrasoft pseudopotentials to the projector augmented-wave method. *Phys. Rev. B* **1999**, *59*, 1758−1775.
(28) Kresse, G.; Furthmüller, J. Efficient iterative schemes for ab initio total-energy calculations using a plane-wave basis set. *Phys. Rev. B* **1996**, *54*, 11169−11186.
(29) Blöchl, P. E. Projector augmented-wave method. *Phys. Rev. B.* **1994**, *50*, 17953−17979.
(30) Perdew, J. P.; Burke, K.; Ernzerhof, M. Generalized Gradient Approximation Made Simple. *Phys. Rev. Lett.* **1996**, *77*, 3865−3868.
(31) Blöchl, P. E.; Jepsen, O.; Andersen, O. K. Improved tetrahedron method for Brillouin-zone integrations. *Phys. Rev. B* **1994**, *49*, 16223−16233.
(32) Teo, J. H.; Strauss, F.; Walther, F.; Ma, Y.; Payandeh, S.; Scherer, T.; Bianchini, M.; Janek, J.; Brezesinski, T. The interplay between (electro)chemical and (chemo)mechanical effects in the cycling performance of thiophosphate-based solid-state batteries. *Mater. Futures* **2022**, *1*, No. 015102.
(33) Walther, F.; Strauss, F.; Wu, X.; Mogwitz, B.; Hertle, J.; Sann, J.; Rohnke, M.; Brezesinski, T.; Janek, J. The Working Principle of a Li_2CO_3/$LiNbO_3$ Coating on NCM for Thiophosphate-Based All-Solid-State Batteries. *Chem. Mater.* **2021**, *33*, 2110−2125.
(34) Randau, S.; Walther, F.; Neumann, A.; Schneider, Y.; Negi, R. S.; Mogwitz, B.; Sann, J.; Becker-Steinberger, K.; Danner, T.; Hein, S.; Latz, A.; Richter, F. H.; Janek, J. On the Additive Microstructure in Composite Cathodes and Alumina-Coated Carbon Microwires for Improved All-Solid-State Batteries. *Chem. Mater.* **2021**, *33*, 1380−1393.
(35) Koerver, R.; Zhang, W.; de Biasi, L.; Schweidler, S.; Kondrakov, A. O.; Kolling, S.; Brezesinski, T.; Hartmann, P.; Zeier, W. G.; Janek, J. Chemo-mechanical expansion of lithium electrode materials − on the route to mechanically optimized all-solid-state batteries. *Energy Environ. Sci.* **2018**, *11*, 2142−2158.
(36) Minnmann, P.; Quillman, L.; Burkhardt, S.; Richter, F. H.; Janek, J. Editors' Choice—Quantifying the Impact of Charge Transport Bottlenecks in Composite Cathodes of All-Solid-State Batteries. *J. Electrochem. Soc.* **2021**, *168*, No. 040537.
(37) Famprikis, T.; Kudu, Ö. U.; Dawson, J. A.; Canepa, P.; Fauth, F.; Suard, E.; Zbiri, M.; Dambournet, D.; Borkiewicz, O. J.; Bouyanfif, H.; Emge, S. P.; Cretu, S.; Chotard, J.-N.; Grey, C. P.; Zeier, W. G.; Islam, M. S.; Masquelier, C. Under Pressure: Mechanochemical Effects on Structure and Ion Conduction in the Sodium-Ion Solid Electrolyte Na3PS4. *J. Am. Chem. Soc.* **2020**, *142*, 18422−18436.
(38) Schneider, C.; Schmidt, C. P.; Neumann, A.; Clausnitzer, M.; Sadowski, M.; Harm, S.; Meier, C.; Danner, T.; Albe, K.; Latz, A.; Wall, W. A.; Lotsch, B. V. Effect of Particle Size and Pressure on the Transport Properties of the Fast Ion Conductor t-Li_7SiPS_8. *Adv. Energy Mater.* **2023**, *13*, No. 2203873.
(39) Dubois, P.; Lelieur, J.; Lepoutre, G. Identification and characterization of lithium polysulfides in solution in liquid ammonia. *Inorg. Chem.* **1988**, *27*, 73−80.
(40) Chivers, T. Ubiquitous trisulphur radical ion $S_3^{-}\cdot$. *Nature* **1974**, *252*, 32−33.
(41) Ruhl, J.; Riegger, L. M.; Ghidiu, M.; Zeier, W. G. Impact of Solvent Treatment of the Superionic Argyrodite Li_6PS_5Cl on Solid-State Battery Performance. *Adv. Energy Sustainability Res.* **2021**, *2*, No. 2000077.
(42) Ziolkowska, D. A.; Arnold, W.; Druffel, T.; Sunkara, M.; Wang, H. Rapid and Economic Synthesis of a Li_7PS_6 Solid Electrolyte from a Liquid Approach. *ACS Appl. Mater. Interfaces* **2019**, *11*, 6015−6021.
(43) Yubuchi, S.; Uematsu, M.; Hotehama, C.; Sakuda, A.; Hayashi, A.; Tatsumisago, M. An argyrodite sulfide-based superionic conductor synthesized by a liquid-phase technique with tetrahydrofuran and ethanol. *J. Mater. Chem. A* **2019**, *7*, 558−566.
(44) Zhou, L.; Park, K.-H.; Sun, X.; Lalère, F.; Adermann, T.; Hartmann, P.; Nazar, L. F. Solvent-Engineered Design of Argyrodite Li_6PS_5X (X = Cl, Br, I) Solid Electrolytes with High Ionic Conductivity. *ACS Energy Lett.* **2019**, *4*, 265−270.
(45) Yubuchi, S.; Uematsu, M.; Deguchi, M.; Hayashi, A.; Tatsumisago, M. Lithium-Ion-Conducting Argyrodite-Type Li_6PS_5X (X = Cl, Br, I) Solid Electrolytes Prepared by a Liquid-Phase Technique Using Ethanol as a Solvent. *ACS Appl. Energy Mater.* **2018**, *1*, 3622−3629.
(46) Dietrich, C.; Weber, D. A.; Sedlmaier, S. J.; Indris, S.; Culver, S. P.; Walter, D.; Janek, J.; Zeier, W. G. Lithium ion conductivity in Li_2S−P_2S_5 glasses − building units and local structure evolution during the crystallization of superionic conductors Li_3PS_4, $Li_7P_3S_{11}$ and $Li_4P_2S_7$. *J. Mater. Chem. A* **2017**, *5*, 18111−18119.
(47) Machida, N.; Yamamoto, H.; Asano, S.; Shigematsu, T. Preparation of amorphous $75L_2S{\cdot}xP_2S_3{\cdot}(25-x)P_2S_5$ (mol%) solid

https://doi.org/10.1021/acsaem.2c03278
ACS Appl. Energy Mater. 2023, 6, 7790−7802

electrolytes by a high-energy ball-milling process and their application for an all-solid-state lithium battery. *Solid State Ionics* **2005**, *176*, 473−479.
(48) Hansen, C. M. *Hansen Solubility Parameters: A User's Handbook*; CRC Press, 2007.
(49) Hansen, C. M. The three dimensional solubility parameter and solvent diffusion coefficient: Their importance in surface coating formulation. Danish Technical Press: 1967.
(50) Reichardt, C.; Welton, T. Appendix A. Properties, Purification, and Use of Organic Solvents. In *Solvents and Solvent Effects in Organic Chemistry*; John Wiley & Sons, 2010; pp 549−586.
(51) PubChem Compound Summary for CID 31254, N-Methylformamide, 2022. https://pubchem.ncbi.nlm.nih.gov/compound/N-Methylformamide. (accessed August 17, 2022).
(52) Yamamoto, K.; Takahashi, M.; Ohara, K.; Phuc, N. H. H.; Yang, S.; Watanabe, T.; Uchiyama, T.; Sakuda, A.; Hayashi, A.; Tatsumisago, M.; Muto, H.; Matsuda, A.; Uchimoto, Y. Synthesis of Sulfide Solid Electrolytes through the Liquid Phase: Optimization of the Preparation Conditions. *ACS Omega* **2020**, *5*, 26287−26294.
(53) Takahashi, M.; Yang, S.; Yamamoto, K.; Ohara, K.; Phuc, N. H. H.; Watanabe, T.; Uchiyama, T.; Sakuda, A.; Hayashi, A.; Tatsumisago, M.; Muto, H.; Matsuda, A.; Uchimoto, Y. Improvement of lithium ionic conductivity of Li3PS4 through suppression of crystallization using low-boiling-point solvent in liquid-phase synthesis. *Solid State Ionics* **2021**, *361*, No. 115568.
(54) Mercier, R.; Malugani, J.-P.; Fahys, B.; Robert, G.; Douglade, J. Structure du tetrathiophosphate de lithium. *Acta Crystallogr., Sect. B: Struct. Crystallogr. Cryst. Chem.* **1982**, *38*, 1887−1890.
(55) Homma, K.; Yonemura, M.; Kobayashi, T.; Nagao, M.; Hirayama, M.; Kanno, R. Crystal structure and phase transitions of the lithium ionic conductor Li_3PS_4. *Solid State Ionics* **2011**, *182*, 53−58.
(56) Kitano, M.; Kuchitsu, K. Molecular Structure of N-Methylformamide as Studied by Gas Electron Diffraction. *Bull. Chem. Soc. Jpn.* **1974**, *47*, 631−634.
(57) Olejnik, S.; Posner, A. M.; Quirk, J. P. The I.R. Spectra of Interlamellar Kaolinite-Amide Complexes—I. The Complexes of Formamide, N-Methylformamide and Dimethylformamide. *Clays Clay Miner.* **1971**, *19*, 83−94.
(58) Suzuki, I. Infrared Spectra and Normal Vibrations of Thioamides. III. N-Methylthioformamide and N-Methylthioacetamide. *Bull. Chem. Soc. Jpn.* **1962**, *35*, 1456−1464.
(59) Brockner, W.; Jendrzok, B.; Menzel, F.; Jensen, V. R.; Ystenes, M. Vibrational spectra and ab initio quantum mechanical calculation of energy, geometry and vibrational frequencies of the oxothiophosphate ions $PO_3S_3^-$, $PO_2S_3^{-2}$ and POS_3^{-3}. *J. Mol. Struct.* **1994**, *319*, 85−100.
(60) Popović, L.; Manoun, B.; de Waal, D.; Nieuwoudt, M. K.; Comins, J. D. Raman spectroscopic study of phase transitions in Li_3PO_4. *J. Raman Spectrosc.* **2003**, *34*, 77−83.
(61) Matsuda, Y.; Kuwata, N.; Okawa, T.; Dorai, A.; Kamishima, O.; Kawamura, J. In situ Raman spectroscopy of Li_xCoO_2 cathode in Li/Li_3PO_4/$LiCoO_2$ all-solid-state thin-film lithium battery. *Solid State Ionics* **2019**, *335*, 7−14.
(62) Kato, A.; Kowada, H.; Deguchi, M.; Hotehama, C.; Hayashi, A.; Tatsumisago, M. XPS and SEM analysis between Li/Li_3PS_4 interface with Au thin film for all-solid-state lithium batteries. *Solid State Ionics* **2018**, *322*, 1−4.
(63) Wenzel, S.; Sedlmaier, S. J.; Dietrich, C.; Zeier, W. G.; Janek, J. Interfacial reactivity and interphase growth of argyrodite solid electrolytes at lithium metal electrodes. *Solid State Ionics* **2018**, *318*, 102−112.
(64) Wood, K. N.; Steirer, K. X.; Hafner, S. E.; Ban, C.; Santhanagopalan, S.; Lee, S.-H.; Teeter, G. Operando X-ray photoelectron spectroscopy of solid electrolyte interphase formation and evolution in Li_2S-P_2S_5 solid-state electrolytes. *Nat. Commun.* **2018**, *9*, No. 2490.
(65) Koerver, R.; Walther, F.; Aygün, I.; Sann, J.; Dietrich, C.; Zeier, W. G.; Janek, J. Redox-active cathode interphases in solid-state batteries. *J. Mater. Chem. A* **2017**, *5*, 22750−22760.
(66) Ma, Y.; Teo, J. H.; Walther, F.; Ma, Y.; Zhang, R.; Mazilkin, A.; Tang, Y.; Goonetilleke, D.; Janek, J.; Bianchini, M.; Brezesinski, T. Advanced Nanoparticle Coatings for Stabilizing Layered Ni-Rich Oxide Cathodes in Solid-State Batteries. *Adv. Funct. Mater.* **2022**, *32*, No. 2111829.
(67) Wang, B.; Liu, J.; Sun, Q.; Li, R.; Sham, T.-K.; Sun, X. Atomic layer deposition of lithium phosphates as solid-state electrolytes for all-solid-state microbatteries. *Nanotechnology* **2014**, *25*, No. 504007.
(68) Appapillai, A. T.; Mansour, A. N.; Cho, J.; Shao-Horn, Y. Microstructure of LiCoO2 with and without "$AlPO_4$" Nanoparticle Coating: Combined STEM and XPS Studies. *Chem. Mater.* **2007**, *19*, 5748−5757.
(69) Ohno, S.; Bernges, T.; Buchheim, J.; Duchardt, M.; Hatz, A.-K.; Kraft, M. A.; Kwak, H.; Santhosha, A. L.; Liu, Z.; Minafra, N.; Tsuji, F.; Sakuda, A.; Schlem, R.; Xiong, S.; Zhang, Z.; Adelhelm, P.; Chen, H.; Hayashi, A.; Jung, Y. S.; Lotsch, B. V.; Roling, B.; Vargas-Barbosa, N. M.; Zeier, W. G. How Certain Are the Reported Ionic Conductivities of Thiophosphate-Based Solid Electrolytes? An Interlaboratory Study. *ACS Energy Lett.* **2020**, *5*, 910−915.
(70) Marchini, F.; Porcheron, B.; Rousse, G.; Blanquer, L. A.; Droguet, L.; Foix, D.; Koç, T.; Deschamps, M.; Tarascon, J. M. The Hidden Side of Nanoporous β-Li_3PS_4 Solid Electrolyte. *Adv. Energy Mater.* **2021**, *11*, No. 2101111.

https://doi.org/10.1021/acsaem.2c03278
ACS Appl. Energy Mater. 2023, 6, 7790−7802